Volume 27
Number 29
7 August 2025
Pages 15241–15804

PCCP

Physical Chemistry Chemical Physics

rsc.li/pccp

25 YEARS ANNIVERSARY

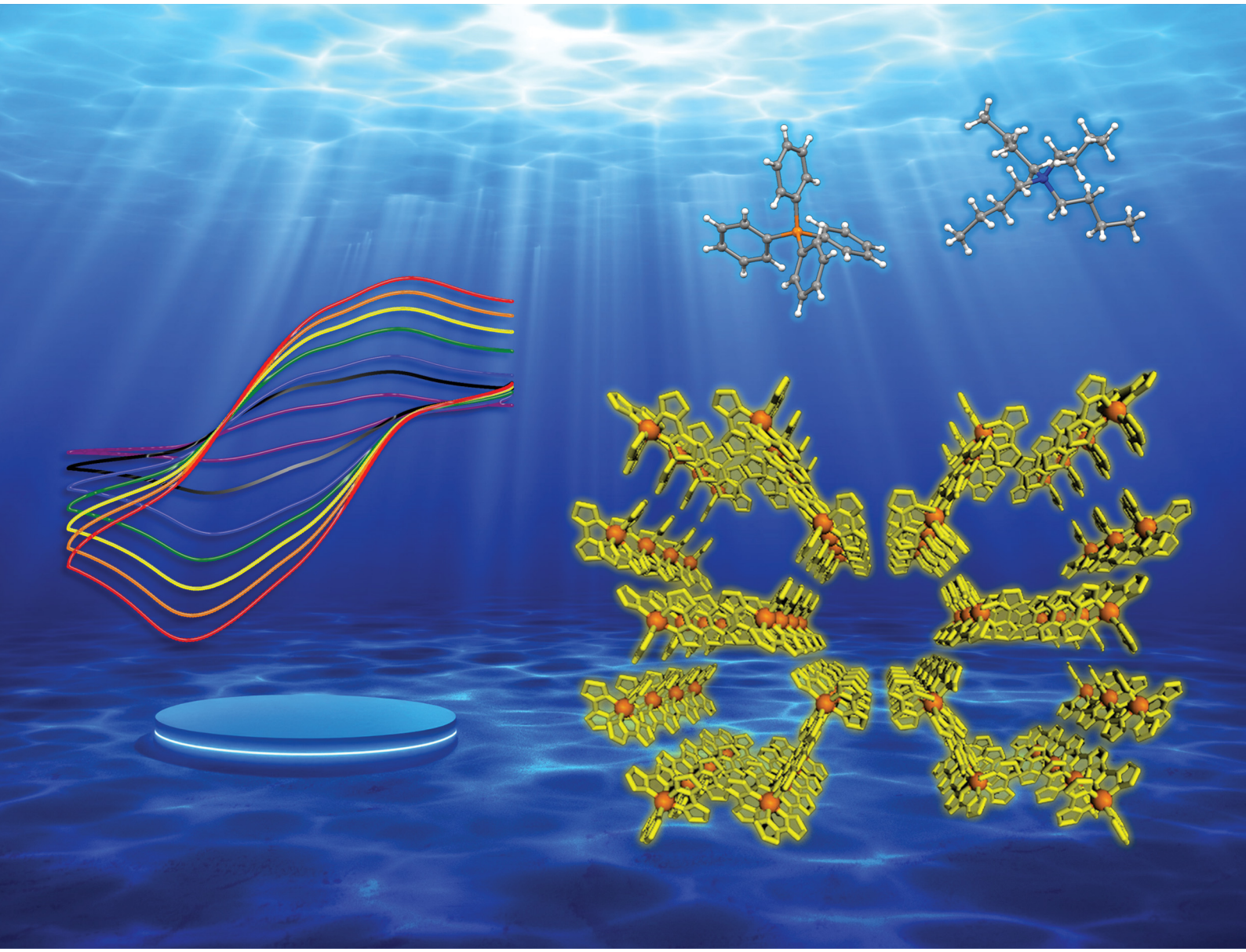

ISSN 1463-9076

ROYAL SOCIETY OF CHEMISTRY

COMMUNICATION

Makoto Tadokoro *et al.*

Two-step insertion/release of electrolytic cations in redox-active hydrogen-bonding nanoporous coordination crystals

PCCP Owner Societies

PCCP

COMMUNICATION

View Article Online
View Journal | View Issue

Cite this: *Phys. Chem. Chem. Phys.*, 2025, **27**, 15310

Received 24th March 2025,
Accepted 29th April 2025

DOI: 10.1039/d5cp01130b

rsc.li/pccp

Two-step insertion/release of electrolytic cations in redox-active hydrogen-bonding nanoporous coordination crystals†

Makoto Tadokoro, *[a] Ryota Nishimura,[a] Hajime Kamebuchi,[b] Fumiya Kobayashi,[a] Jun Miyazaki[c] and Masa-aki Haga[d]

Solid-state cyclic voltammetry (CV) of redox-active H-bonding $\{[Ru^{III}(Hbim)_3]\}_n$ (1) 1-D nanoporous crystals was performed using single crystals in MeCN solutions containing seven electrolyte cations with different effective ionic radii (EIRs). Two cations must be included to every nanochannel unit in $\{[Ru^{II}Ru^{II}]^{2-}\}$ reductive states by a two-step and multi-electron transfer reaction through the $\{[Ru^{III}Ru^{II}]^{-}\}$ mixed-valency state. This study is the first to use solid-state CV to determine the EIR limitation of cations confinable in these crystals.

Self-organising materials such as metal–organic frameworks (MOFs), covalent organic frameworks (COFs), and hydrogen-bonded (H-bonded) organic frameworks (HOFs) have attracted attention over the past decade as functional nanoporous materials.[1] These materials have robust and regular crystalline nanochannel spaces created by molecular designs and can store and separate gases such as CO_2, O_2, and CH_4;[2] hence, they are useful for the insertion/release of active small molecules for a catalytic reaction.[3] In addition, MOFs contain central transition-metal ions with both redox-active[4] and magnetic[5] behaviours. Therefore, they can be used to construct nanoporous frameworks.

Recently, several MOF-based conductors that utilise intermolecular charge-transfer interactions between metal ions and redox-active ligands have been developed.[6] Their conductive mechanisms involve electron flow through the spaces of porous frameworks or conjugated π-electron ligand systems. For example, Prussian blue (PB) ($[\{Fe^{II}–CN–Fe^{III}–CN\}M^{+}]_n$), a conductive MOF discovered more than 300 years ago, has the mixed-valency states of Fe^{2+}/Fe^{3+} bridged by CN^- π-conjugated ligands.[7] The PB crystals exhibit a blue colour owing to the optical charge-transfer transition from Fe^{2+} to Fe^{3+}. Furthermore, PB demonstrates semiconductive behaviour. Alkali and alkaline earth metal ions can be inserted into and released from the PB lattice spaces through electrochemical redox reactions induced by solid-state cyclic voltammetry (CV).[8] Solid-state CV with electrolyte salts containing Rb^+, Cs^+, or NH_4^+ revealed that the metal (M^+) ions can be reversibly inserted into and released from three-dimensional vacant PB lattices more than 10^3 times. However, for Li^+, Na^+, or Ba^{2+} with a large hydrate radius or +2 valence state, the observed current value decreased for every sweep, indicating the decomposition of the PB lattice. Owing to their ion and electron conductivities, such electron-conductive MOFs have wide applications in information transmission systems[9] and supercapacitors.[10]

The crystal of $\{[Ru^{III}(Hbim)_3]\}_n$ (**1**) ($=[\{Ru^{III}Ru^{III}\}^{0}]_n$, where $Hbim^-$ = 2,2′-biimidazolate monoanion),[11] entirely connected by only H-bonds of Ru^{III} complexes $[Ru^{III}(Hbim)_3]$, is a self-organized *quasi*-one-dimensional (1-D) nanoporous crystal. All the π-electron interactions between the metal complexes in $\{[Ru^{III}(Hbim)_3]\}_n$ are disrupted by H-bonds connected through only σ-orbital bonding interactions. The other intermolecular interactions are only weak van der Waals interactions. Fig. 1a shows the solid-state CV curve of **1** with a large reversible redox current when several single crystals of **1** were placed on the surface of a Pt working electrode (ϕ = 1.5 mm) covered with only a membrane filter (ϕ = 0.3 μm) (Fig. S1, ESI†). This is attributed to the solid-state proton-coupled electron transfer (S-PCET) between Ru^{II} and Ru^{III} complexes in **1**. A previous study has synthesised the mixed-valency crystals of $\{[Ru^{II}(H_2bim)(Hbim)_2]$-$[Ru^{III}(bim)(Hbim)_2]$ $(K(BnOMe)_6)\}_n$ (**2**) ($=[\{Ru^{II}Ru^{III}\}^{-}]_n$) and reported the corresponding DC conductivity to be 8.01×10^{-6} S cm^{-1} (277 K), which indicated the semiconductive behaviour[11] (Fig. S2, ESI†). The aforementioned study was the first to report that H-bonded protons (H^+) contribute to the electrical conductivity of a crystal through S-PCET between valence states in the Ru^{II} and Ru^{III} complexes.

[a] *Department of Chemistry, Faculty of Science, Tokyo University of Science, Kagurazaka 1–3, Shinjuku-ku, Tokyo 162-8601, Japan. E-mail: tadokoro@rs.tus.ac.jp*
[b] *Department of Chemistry, College of Humanities and Sciences, Nihon University, Sakurajyosui 3–25-40, Setagaya-ku, Tokyo 156-8550, Japan*
[c] *Department of Natural Sciences, School of Engineering, Tokyo Denki University, Senjuasahi-cho 5, Adachi-ku, Tokyo, 120-8551, Japan*
[d] *Department of Applied Chemistry, Faculty of Science and Technology, Chuo University, Korakuen, Chuo-ku, Tokyo 112-8551, Japan*

† Electronic supplementary information (ESI) available. See DOI: https://doi.org/10.1039/d5cp01130b

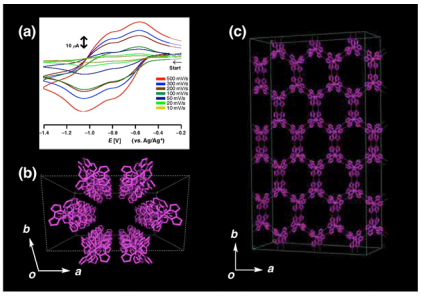

Fig. 1 (a) Solid-state CV of the single crystals of 1 in MeCN with $^{n}Bu_4NPF_6$ as the electrolyte salt. The velocities were changed from 10 to 500 mV s^{-1}. (b) Down view along the *c* axis showing the 1-D nanochannel unit. (c) View parallel to the *ab* plane showing the 2-D honeycomb sheet structure formed by H-bonds between the $[Ru^{III}(Hbim)_3]$ of **1**.

We have previously reported that crystal **1** is reversibly reduced and oxidized on the electrode interface by solid-state CV and shows a two-step and multi-electron transfer reaction ($[\{Ru^{III}Ru^{III}\}^{0}]_n \rightleftarrows [\{Ru^{II}Ru^{III}\}^{-}]_n \rightleftarrows [\{Ru^{II}Ru^{II}\}^{2-}]_n$).[11] The current in **1** flows internally *via* a series of sequential S-PCET reactions until the reduced state of $[\{Ru^{II}Ru^{II}\}^{2-}]_n$ is reached. As **1** is completely reduced, up to two electrolytic cations must be inserted into each of the vacant channel unit of the 1-D nanochannel due to charge compensation. However, owing to the size limitation of the channel pore (~2 nm) in **1**, the insertion of two cations may be incomplete, depending on the size, shape, and characteristics of the cations. In this study, we theoretically calculated the effective ionic radius (EIRs) for each cation. Then, we employed solid-state CV to investigate the insertion/release reactions of seven different counter-cations, varying in size, shape, and characteristics, for the porous channel with a diameter of ~2 nm of **1**. This study is the first to use solid-state CV measurements of single crystals to discover the size limitation of electrolyte cations that can be confined to nanoporous crystals formed from redox-active H-bonding metal complexes *via* the S-PCET reaction.

Fig. 1b and c show the structure of a nanoporous single crystal of **1**, in which the H-bonded Ru^{III} complexes ($[Ru^{III}(Hbim)_3]$) are linked only by intermolecular H-bonds and have the reversible one-step and one-electron transfer for the redox activity of Ru^{3+}/Ru^{2+} in MeCN solution. According to single-crystal X-ray structural analysis, **1** is constructed by the stacking of the repeating units of 2-D honeycomb sheet structures (Fig. S3, ESI†), in which two Δ and Λ optical isomers of $[Ru^{III}(Hbim)_3]$ alternately form a triad with complementary two-point H-bonds. The hexagonal cavities in the honeycomb sheets are stacked to give large 1-D nanochannels of ~2 nm width. The side walls of the 1-D nanochannels are formed by the alternative stacking of the Δ and Λ isomers of $[Ru^{III}(Hbim)_3]$ ($Ru^{3+}\cdots Ru^{3+}$ = 7.777(6) Å) to afford a woven ribbon structure. The solid-state CV measurements of the single crystals of **1** show a two-step and multi-electron transfer reaction of $\{[Ru^{III}Ru^{III}]^{0}\}_n \leftrightarrows \{[Ru^{II}Ru^{III}]^{-}\}_n \leftrightarrows \{[Ru^{II}Ru^{II}]^{2-}\}_n$ ($E^{1}_{1/2}$ = −0.61 V, $E^{2}_{1/2}$ = −0.92 V, *vs.* Ag/Ag^+ in MeCN with 0.1 M $^{n}Bu_4NPF_6$). Before deprotonation, the mononuclear complex $[Ru^{II}(H_2bim)_3](PF_6)_2$ exhibited only a reversible one-step and one-electron transfer of $[Ru^{II}(H_2bim)_3]^{2+} \leftrightarrows [Ru^{III}(H_2bim)_3]^{3+}$ ($E_{1/2}$ = 0.33 V *vs.* Ag/Ag^+ in MeCN with 0.1 M $^{n}Bu_4NPF_6$), as measured by solution CV. (Fig. S4, ESI†). Additionally, the solid-state CV measurements revealed that both Ru^{II} and Ru^{III} states coexist on the crystal interfaces because exactly half of the $[Ru^{III}(Hbim)_3]$ complexes were reduced to $[Ru^{II}(Hbim)_3]^{-}$ in the electric double layer on the electrode surface (Fig. S5, ESI†). The $\{[Ru^{II}Ru^{III}]^{-}\}_n$ mixed-valency state in **1** was reversible. Hence, a rapid PT must be facilitated after the electron transfer (ET) from the electrode surface.

During the reductive reaction of a Ru^{III} complex to Ru^{II} one for **1**, one H^+ moves through one of the three H-bonds from $[Ru^{III}(Hbim)_3]$ to the adjacent $[Ru^{II}(Hbim)_3]^{-}$, forming $[Ru^{III}(bim)(Hbim)_2]^{-}$ and $[Ru^{II}(H_2bim)(Hbim)_2]^{0}$, respectively. Thus, the macroscopic mixed-valency state of $\{[Ru^{II}Ru^{III}]^{-}\}_n$ is stabilised as $\{[Ru^{II}(H_2bim)(Hbim)_2][Ru^{III}(bim)(Hbim)_2]^{-}\}_n$ (Fig. S6, ESI†). During the redox reaction, electrolytic cations move into and out of the electrolyte solution through the opening gates of nanochannels of **1** owing to charge compensation. This suggests that ET is a rate-determining step for a diffusion process of the electrolytic cations to the inside crystal. Before the redox reaction of **1**, $^{n}Bu_4N^+$ cations do not enter the void spaces in the hexagonal nanochannels, containing the solvent molecules because of the neutral repeating units of $\{[Ru^{III}Ru^{III}]^{0}\}_n$. However, in the mixed-valency state of $\{[Ru^{II}Ru^{III}]^{-}\}_n$, half of the Ru^{III} complexes are reduced to Ru^{II} ones by electrons. Consequently, one $^{n}Bu_4N^+$ is inserted to each nanochannel unit of **1** to compensate for the −1 charge in the mixed-valency state. In addition, the $\{[Ru^{II}Ru^{III}]^{-}\}_n$ state is reduced to $\{[Ru^{II}Ru^{II}]^{2-}\}_n$ by electrons, generating the −2 charge in each nanochannel unit. As a result, two $^{n}Bu_4N^+$ are inserted into each of the nanochannel unit for charge compensation. As **1** reversibly undergoes a two-electron redox reaction in each nanochannel unit on a solid-state CV set-up, two $^{n}Bu_4N^+$ would move into and out of each nanochannel unit. However, for electrolyte salts containing large bulky cations, the wavy shapes of the redox peaks in the solid-state CV measurement would change depending on the capture/release mechanism for their cations to the nanoporous crystal of **1**. Therefore, in this study, we have investigated the peak changes in the solid-state CV curves of seven electrolyte salts with cations of different sizes, shapes, and characteristics.

Table 1 presents the EIRs[12] of seven counter-cations containing the electrolyte salts used in solid-state CV measurements. The EIRs were calculated based on the geometry optimization for each of the seven cations in the gas phase and PCM (polarizable continuum model) condition for MeCN solvation by using the B3LYP/6-311+G(d) basis set included in the Gaussian 16 software package.[13] The temperature was set at 298.15 K for every calculation. The EIRs are optimized between the center of N atoms and the terminal H atoms of C atoms in the all-*trans* conformation of various NR_4^+ ions, and between the center of a P atom and H atom on the 4-position of a phenyl ring in PPh_4^+, whose initial geometry (or structure) is referred from the 3-D conformer shown in PubChem[14] (Fig. S7, ESI†).

The seven counter-cations, which exist as electrolyte salts with Br^- anions, were used in the solid-state CV measurements as 0.1 M MeCN solution. The cations were found to have a wide range of sizes and characteristics, ranging from a smaller $^{n}Pr_4N^+$ (~4.75 Å) to a larger $^{n}Oct_4N^+$ (~11.17 Å), and a softer R_4N^+ (R = *n*-propyl (^{n}Pr), *n*-butyl (^{n}Bu) (~6.05 Å), *n*-pentyl (^{n}Pen)

Table 1 Effective ionic radii of electrolytic cations

Abbreviations	Ph_4P^+	$^nPr_4N^+$	$^nBu_4N^+$	$^nPen_4N^+$	$^nHex_4N^+$	$^nHep_4N^+$	$^nOct_4N^+$
Effective ionic radii[a] (EIRs)	~5.69 Å	~4.75 Å	~6.05 Å	~7.32 Å	~8.61 Å	~9.88 Å	~11.17 Å
Formula	$C_{24}H_{20}P^+$	$C_{12}H_{28}N^+$	$C_{16}H_{36}N^+$	$C_{20}H_{44}N^+$	$C_{24}H_{52}N^+$	$C_{28}H_{60}N^+$	$C_{32}H_{68}N^+$
Molecular weight	339.40	186.36	242.47	298.58	354.69	410.80	466.80

[a] We performed the geometry optimization for those molecules in the PCM condition (solvent: Acetonitrile) using the B3LYP/6-311+G(d) basis set included in the Gaussian 16 software package.[12] The temperature was set at 298.15 K every calculation.

(~7.32 Å), *n*-hexyl (^{n}Hex) (~8.61 Å), *n*-heptyl (^{n}Hep) (~9.88 Å), and *n*-octyl (^{n}Oct)) to harder Ph_4P^+ (~5.69 Å). The solid-state CV measurements were conducted until two cations are inserted/released in each 1-D nanochannel unit of **1** during the redox reaction of $\{[Ru^{III}Ru^{III}]^0\}_n \leftrightarrows \{[Ru^{II}Ru^{III}]^-\}_n \leftrightarrows \{[Ru^{II}Ru^{II}]^{2-}\}_n$. As PPh_4Br exhibited a different trend, we compared the primary ($E^1_{1/2}$) and secondary ($E^2_{1/2}$) potentials of the solid-state CV redox reactions of **1** in MeCN. Notably, $^nPr_4N^+$ ($E^1_{1/2} = -0.66$ V, $E^2_{1/2} = -0.93$ V), $^nBu_4N^+$ ($E^1_{1/2} = -0.61$ V, $E^2_{1/2} = -0.92$ V), and $^nPen_4N^+$ ($E^1_{1/2} = -0.64$ V, $E^2_{1/2} = -0.97$ V) demonstrated reversible two-step and multi-electron transfer processes with similar current areas and shapes for $E^1_{1/2}$ and $E^2_{1/2}$ through the $\{[Ru^{II}Ru^{III}]^-\}_n$ mixed-valency state. The results suggest that three cations with a smaller EIR than that of $^nHex_4N^+$ can be reversibly inserted into and released from each 1-D nanochannel unit of **1** in a sequential manner owing to charge compensation (Fig. 2a). In contrast, three cations with EIRs larger than that of $^nPen_4N^+$, that is $^nHex_4N^+$ ($E^1_{1/2} = -0.65$ V, $E^2_{1/2} = -1.11$ V), $^nHep_4N^+$ ($E^1_{1/2} = -0.66$ V, $E^2_{1/2} = -1.09$ V), and $^nOct_4N^+$ ($E^1_{1/2} = -0.66$ V, $E^2_{1/2} = -0.97$ V), showed almost no changes in their redox potentials for $E^1_{1/2}$ and $E^2_{1/2}$. Nevertheless, the secondary redox waves of $^nHex_4N^+$, $^nHep_4N^+$, and $^nOct_4N^+$ were sharper, and the current areas gradually decreased (Fig. 2b). To investigate whether the electrolytic anions of $^nBu_4NX$ influence the redox reactions, we performed solid-state CV measurements of **1** in four electrolyte salts containing different anions (X^- = PF_6^-, Br^-, BF_4^-, and ClO_4^-). The four CV curves of **1** in $^nBu_4NPF_6$ ($E^1_{1/2} = -0.61$ V, $E^2_{1/2} = -0.92$ V), $^nBu_4NBr$ ($E^1_{1/2} = -0.66$ V, $E^2_{1/2} = -0.89$ V), $^nBu_4NBF_4$ ($E^1_{1/2} = -0.67$ V, $E^2_{1/2} = -0.95$ V), and $^nBu_4NClO_4$ ($E^1_{1/2} = -0.66$ V, $E^2_{1/2} = -0.95$ V) were almost comparable. This indicates that the changes in the $E^1_{1/2}$ and $E^2_{1/2}$ redox reactions of **1** were influenced only by the electrolytic cations.

Fig. 2 shows the solid-state CV curves of **1** in MeCN solutions of $^nPen_4NBr$ and $^nOct_4NBr$. The secondary oxidation peak E^2_a in the CV curve of **1** in $^nPen_4NBr$ showed the largest half-width potential ΔE^2_a(HW) (442 mV), whereas that of **1** in $^nOct_4NBr$ was 52 mV, which is nearly 1/10th of the current area. The ratio of the current area of the primary reduction peak E^1_c (C_1) to that of the secondary oxidation peak E^2_a (C_2) (*i.e.* C_2/C_1) decreased from 1.37 to 0.30, which is the EIR region between $^nPen_4N^+$ (~7.32 Å) and $^nHex_4N^+$ (~8.61 Å). The line graphs of ΔE^2_a(HW) in Fig. 3a also show the separation between $^nPen_4N^+$ and $^nHex_4N^+$, which highlights the significance of EIRs of the R_4N^+ cations. In the case of the three cations smaller than $^nHex_4N^+$, the C_2/C_1 values were greater than 1.0, and the ΔE^2_a(HW) values were ~400 mV on average. In contrast, for three cations larger than $^nPen_4N^+$, the C_2/C_1 approximately decreased to ~0.35, and the ΔE^2_a(HW) decreased by ~70 mV on average. This is because the two larger cations cannot be accommodated in the 1-D nanochannel unit of **1** in the $\{[Ru^{II}Ru^{II}]^{2-}\}_n$ reduction state; however, the secondary cations can be partially inserted into or incompletely adsorbed onto the crystal surface of **1**. Furthermore, the current values in the secondary redox waves partially decreased during the reduction of the mixed-valency $\{[Ru^{II}Ru^{III}]^-\}_n$ state to the reduced $\{[Ru^{II}Ru^{II}]^{2-}\}_n$ state because only a few larger secondary cations could be completely inserted into the nanochannel units. During the E^2_a oxidation reaction, the partially inserted cations were immediately released during the partial oxidation of the $\{[Ru^{II}Ru^{II}]^{2-}\}_n$ states to the $\{[Ru^{II}Ru^{III}]^-\}_n$ state. Generally, as ΔE^2_a(HW) on the CV curve becomes sharper, the redox reaction occurs faster. For example, for the largest cation $^nOct_4N^+$, the secondary cation in the $\{[Ru^{II}Ru^{II}]^{2-}\}_n$ state was incompletely adsorbed on the crystal surface of **1** or partially trapped in the 1-D nanochannel units. Therefore, these cations were rapidly released immediately after the partial oxidation of $\{[Ru^{II}Ru^{II}]^{2-}\}_n$ to $\{[Ru^{II}Ru^{III}]^-\}_n$. Fig. 3b shows the C_2/C_1 and ΔE^2_a(HW) values of the four electrolyte salts of $^nBu_4N^+$ with different anions (Br^-, ClO_4^-, PF_6^-, and BF_4^-). Every C_2/C_1 value was greater than 1.0, and the ΔE^2_a(HW) was ~400 mV on average, indicating that changes in the CV curves were solely caused by the cations.

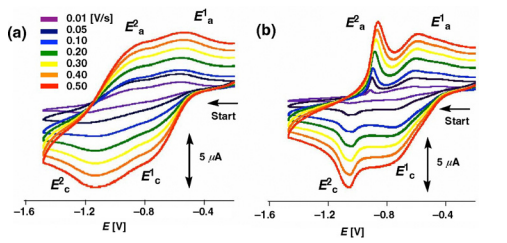

Fig. 2 Solid-state CV images of **1** in MeCN solutions of (a) $^nPen_4NBr$ and (b) $^nOct_4NBr$ electrolyte salts. The velocity was changed from 0.01 to 0.5 V s^{-1} (*vs.* Ag/Ag^+, WE: glassy carbon, RE: Pt wire).

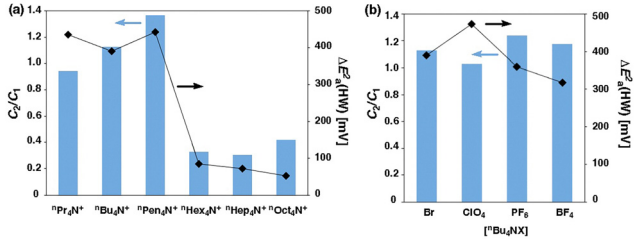

Fig. 3 Ratios of the current areas of the primary reduction peaks E^1_c (C_1) to those of the secondary oxidation peaks E^2_a (C_2) of the solid-state CV curves as bar graphs and the corresponding half-width potentials ΔE^2_a(HW) as line graphs of (a) **1** in six electrolyte salts with R_4N^+ cations of different EIRs and (b) **1** in four electrolyte salts with different X^- anions of $^nBu_4N^+$.

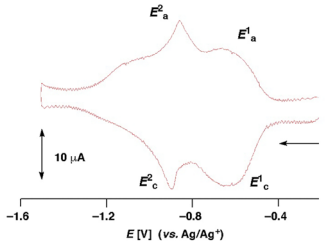

Fig. 4 Semi-differential solid-state CV curve of **1** measured in MeCN solution with the Ph_4PBr electrolyte salt.

Unlike other R_4N^+ electrolytic cations, Ph_4P^+ contains four rigid phenyl groups bonded to a phosphorous (P) atom, has a spherical shape as a whole, and is one of the cations with the smaller EIR (∼5.69 Å) among the seven cations with a relatively large molecular weight (M_W = 339.40). The semi-differential solid-state CV curve ($E^1_{1/2}$ = −0.62 V, $E^2_{1/2}$ = −0.89 V) in the MeCN solution containing PPh_4Br resembled the characteristic CV curve in solution with the three larger NR_4^+ cations compared to $^n Pen_4N^+$ one (Fig. 4). The semi-differential representation excludes a diffuse component from the solid-state CV curve. In the $\{[Ru^{III}Ru^{III}]^0\}_n$ state of **1**, each 1-D nanochannel unit is initially filled with only MeCN; however, the primary Ph_4P^+ cation is inserted into each nanochannel unit through E^1_c reduction. Nevertheless, the secondary Ph_4P^+ cation cannot be completely accommodated in the nanochannel unit during the subsequent $E_c{}^2$ reduction. Accordingly, the line shape of the oxidation E^2_a narrowed (ΔE^2_a(HW) = 80 mV), and the C_2/C_1 value was 0.16. This value is comparable to that of the larger $^n Hex_4N^+$ (EIR = ∼8.61 Å), even though PPh_4^+ is much smaller (EIR = ∼5.69 Å). This observation could be attributed to the flexible and deformable alkyl chains of R_4N^+, which, unlike Ph_4P^+, has a rigid spherical structure. Therefore, although the EIR is relatively small, two Ph_4P^+ cations cannot be completely accommodated in one 1-D nanochannel unit. A previous study reported that the energy density and power capacity of supercapacitor materials, comprising nanoporous carbons, depended on the uptake quantities of NEt_4^+ cations. The amount of NEt_4^+ cations with four ethyl chains anomalously increased in the nanopores with the size-distribution of less than ∼1 nm; this was attributed to desolvation and deformation of electrolytic NEt_4^+ cations.[15] However, compared to NR_4^+ with long alkyl chains, PPh_4^+ cations are rigid and cannot be deformed; therefore, despite its small EIR, PPh_4^+ behaves similarly to $^n Hex_4N^+$, whose EIR is ∼3 Å larger.

In summary, $^n Pr_4N^+$, $^n Bu_4N^+$, and $^n Pen_4N^+$ cations were completely inserted as two cations into each 1-D nanochannel unit of **1** after the reduction of **1** to $\{[Ru^{II}Ru^{II}]^{2-}\}_n$. In contrast, only one larger $^n Hex_4N^+$, $^n Hep_4N^+$, and $^n Oct_4N^+$ cation and the smaller but rigid PPh_4^+ cation could be completely inserted into each 1-D nanochannel unit in the mixed-valency state of $\{[Ru^{II}Ru^{III}]^-\}_n$, while the other secondary cations were only partially inserted into the remaining space of the 1-D nanochannel units. This resulted in a smaller and sharper secondary oxidation peak of E^2_a. While two PPh_4^+ cations were restricted in each nanochannel unit owing to their rigid structure, two $^n Pen_4N^+$ cations with flexible, long alkyl chains were not restricted. This finding has implications increasing the energy densities of capacitors and in realizing the first functionalization utilising the S-PCET reaction.

Data availability

The data that support the findings of this study are available within the part of the ESI.†

Conflicts of interest

There are no conflicts to declare.

Acknowledgements

This work was supported by the JSPS KAKENHI Grant-in-Aid for Scientific Research (B) JP23H01979 (M. T.) from the Ministry of Education, Culture, Sports, Science, and Technology, Japan.

Notes and references

1 (*a*) O. M. Yaghi, G. Li and H. Li, *Nature*, 1995, **378**(6558), 703–706; (*b*) S. Kitagawa, R. Kitaura and S. Noro, *Angew. Chem., Int. Ed.*, 2004, **43**, 2334–2375; (*c*) Y. Yang, Z. Sun, Y. Wu, Z. Liang, F. Li, M. Zhu and J. Liu, *Small*, 2024, **20**, 2401457; (*d*) A. P. Côté, A. I. Benin, N. W. Ockwig, M. O'Keeffe, A. J. Matzger and O. M. Yaghi, *Science*, 2005, **310**, 1166–1170; (*e*) Y. He, S. Xiang and B. Chen, *J. Am. Chem. Soc.*, 2011, **133**, 14570–14573.
2 D. Alezi, Y. Belmabkhout, M. Suyetin, P. M. Bhatt, J. Weselinski, V. Solovyeva, K. Adil, I. Spanopoulos, P. N. Trikalitis, A.-H. Emwas and M. Eddaoudi, *J. Am. Chem. Soc.*, 2015, **137**, 13308–13318.
3 J. Liu, N. Wang and L. Ma, *Chem. – Asian J.*, 2020, **15**, 325–439.
4 S. A. A. Razavi, W. Chen, H.-C. Zhou and A. Morsali, *Coord. Chem. Rev.*, 2024, **517**, 216004.
5 A. E. Thorarinsdottir and T. D. Harris, *Chem. Rev.*, 2020, **120**, 8716–8787.
6 K. O. Kirlikovali, S. Goswami, M. R. Mian, M. D. Krzyaniak, M. R. Wasielewski, J. T. Hupp, P. Li and O. K. Farha, *ACS Mater. Lett.*, 2022, **4**, 128–135.
7 N. Kitchamsetti, *J. Energy Storage*, 2023, **73**, 108958.
8 L. S. Xie, G. Skorupskii and M. Dinca, *Chem. Rev.*, 2020, **120**, 8536–8580.
9 S. Shang, C. Du, Y. Liu, M. Liu, X. Wang, W. Gao, Y. Zou, J. Dong, Y. Liu and J. Chen, *Nat. Commun.*, 2022, **13**, 7599.
10 J. Su, W. He, X.-M. Li, L. Sun, H.-Y. Wang, Y.-Q. Lan, M. Ding and J.-L. Zuo, *Matter*, 2020, **2**, 711–722.
11 M. Tadokoro, H. Hosoda, T. Inoue, A. Murayama, K. Noguchi, A. Iioka, R. Nishimura, M. Itoh, T. Sugaya, H. Kamebuchi and M. Haga, *Inorg. Chem.*, 2017, **56**, 8513–8526.
12 R. D. Shannon, *Acta Cryst.*, 1976, **A32**, 751–767.
13 *Gaussian16, Revision C.01*, Gaussian, Inc., Wallingford, CT, 2016.
14 Tetraphenylphosphonium 3-D Conformer, **https://pubchem.ncbi.nlm.nih.gov/compound/164912#section=3D-Conformer**, (accessed October 2013).
15 J. Chmiola, G. Yushin, Y. Gogotsi, C. Portet, P. Simon and P. L. Taberna, *Science*, 2006, **313**, 1760–1763.